Editors' Suggestion

Revealing pressure-driven structural transitions in the hybrid improper ferroelectric $Sr_3Sn_2O_7$

K. A. Smith,[1] S. P. Ramkumar,[2] N. C. Harms,[1] A. J. Clune,[1] X. Xu,[3] S.-W. Cheong,[3] Z. Liu,[4] E. A. Nowadnick,[2] and J. L. Musfeldt[1]

[1]*Department of Chemistry, University of Tennessee, Knoxville, Tennessee 37996, USA*
[2]*Department of Materials Science and Engineering, University of California, Merced, California 95343, USA*
[3]*Department of Physics and Astronomy, Rutgers University, Piscataway, New Jersey 08854, USA*
[4]*Department of Physics, University of Illinois at Chicago, Illinois 60607-7059, USA*

(Received 18 June 2021; revised 23 July 2021; accepted 28 July 2021; published 12 August 2021)

We combine diamond anvil cell techniques and synchrotron-based infrared spectroscopy with a detailed symmetry analysis and lattice dynamics calculations to uncover a series of pressure-induced structural phase transitions in the hybrid improper ferroelectric $Sr_3Sn_2O_7$. The microscopic character of each high-pressure phase is determined by comparing the measured spectrum with the predicted vibrational patterns of several related but distinct candidate space groups. Our analysis reveals a sequence of pressure-induced transitions from $A2_1am \leftrightarrow Pnab \leftrightarrow Acaa \leftrightarrow I4/mmm$ at room temperature. Remarkably, this space group progression matches the sequence of temperature-dependent structural transitions observed in $Sr_3Sn_2O_7$ between 77 and 1000 K. Other hybrid improper ferroelectrics display a similar set of temperature transitions, suggesting that pressure and probably strain will be very effective tuning parameters for this entire class of materials.

DOI: 10.1103/PhysRevB.104.064106

I. INTRODUCTION

The discovery of hybrid improper ferroelectricity in layered perovksite oxides over the past decade has led to a number of new and exciting room-temperature ferroelectrics, particularly in the $n = 2$ Ruddlesden-Popper $A_3B_2O_7$ family of materials [1–6]. The key feature of hybrid improper ferroelectricity [1,2,7] is a coupling between the polarization and two other structural order parameters, which typically are rotations of the corner-connected network of metal oxide octahedra. The first experimentally confirmed hybrid improper ferroelectric was $Ca_3Ti_2O_7$ [3], and subsequent investigations of its domain and domain wall structure revealed a complex network of domain wall vortices and antivortices [8,9] as well as unusual Néel-type walls [10]. Further studies on $Ca_3Ti_2O_7$ [8] and other hybrid improper ferroelectrics such as $Sr_3Zr_2O_7$ [6] and $Sr_3Sn_2O_7$ [4,6,11–13] demonstrate that their crystal structures are very sensitive to external stimuli, and by varying chemical composition or temperature, a range of structural phases are accessible. Moreover, the Curie temperature T_C can be related to the tolerance factor for a variety of materials in this family [6]. Despite predictions for negative thermal expansion and other exotic properties under compression [8], experimental investigations of these materials under pressure remain quite rare, which is surprising given that pressure is known to directly manipulate bond lengths and bond angles in perovskites [14,15]. In particular, the structural phases that may be accessed under compression and their relation to the temperature-dependent phase transitions remain underexplored.

$Sr_3Sn_2O_7$ is a superb platform with which to examine these ideas. This system is a room-temperature ferroelectric with a 1.15 $\mu C/cm^2$ remnant polarization along [110] and the smallest coercive field of all currently known hybrid improper ferroelectrics [13]. Second harmonic generation, x-ray, and neutron diffraction measurements highlight a ferroelectric-paraelectric structural phase transition at 410 K from a polar $A2_1am$ ground state to a phase with $Pnab$ symmetry [6]. At higher temperatures there are further transitions to $Acaa$ symmetry ($\approx$ 700 K) and finally to $I4/mmm$ ($\approx$ 900 K) [6]. This sequence of structural phases arise from the condensation/extinction of different combinations of octahedral rotations. Figure 1 displays the structure of $Sr_3Sn_2O_7$ and the relationship between the octahedral rotations (and other structural distortions). The $n = 2$ Ruddlesden-Popper structure consists of slabs of two ABO_3 perovskite layers, separated by AO rocksalt layers. The high-symmetry undistorted parent structure has $I4/mmm$ symmetry. The condensation of an out-of-phase ($a^-a^-c^0$ in Glazer notation) octahedral rotation that transforms like the X_3^- irreducible representation of $I4/mmm$ and an in-phase ($a^0a^0c^+$) octahedral rotation that transforms like X_2^+ establishes the $A2_1am$ symmetry of the ground state. The polarization, which arises primarily from Sr displacements, then is induced via a coupling to these octahedral rotations, which is the key feature of the hybrid improper mechanism. The paraelectric $Pnab$ phase arises from a similar mechanism, except now the combination of the $a^-a^-c^0$ rotation and an out-of-phase $a^0a^0c^-$ rotation with symmetry X_1^- establishes $Pnab$ and induces a third distortion with symmetry M_5^+. Significantly, the M_5^+ distortion also consists mainly of Sr displacements, although their amplitudes exactly cancel within each perovskite slab. Finally, the $Acaa$ phase results from the $a^0a^0c^-$ rotation alone.

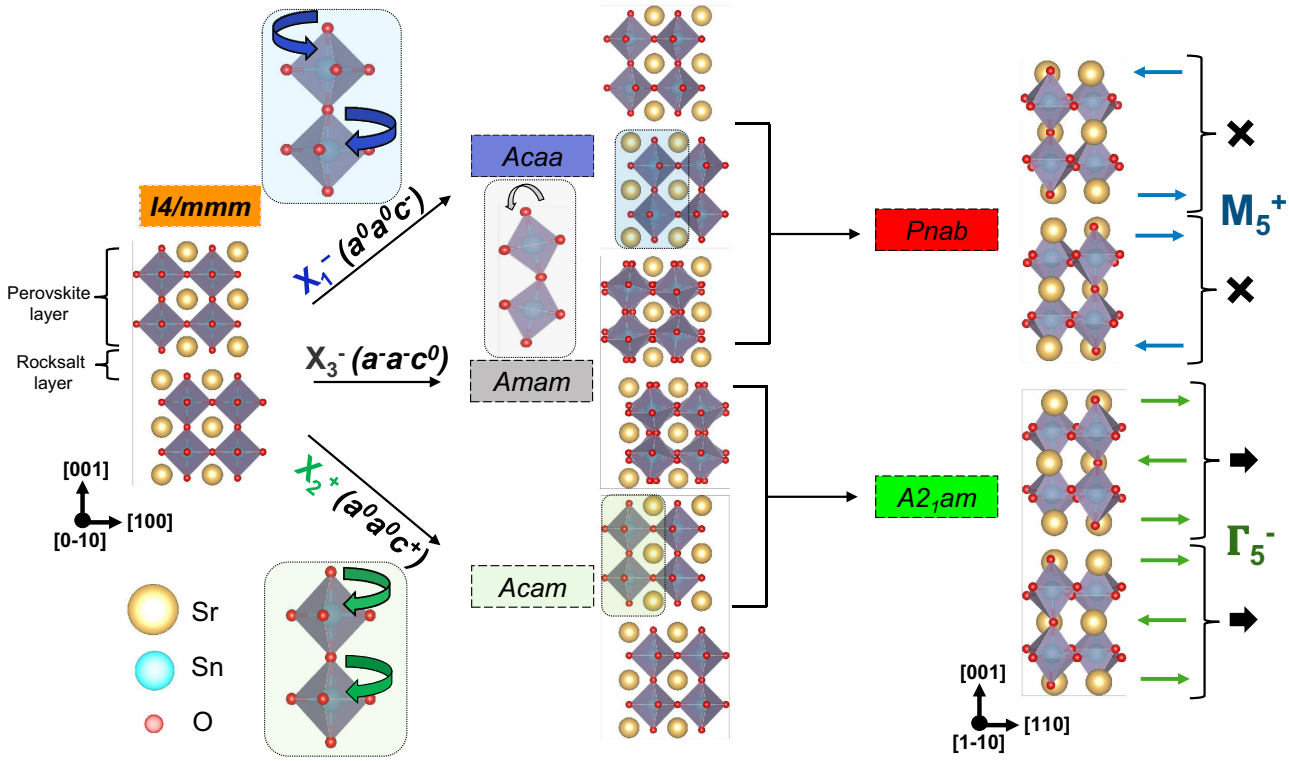

FIG. 1. Structural phases of $Sr_3Sn_2O_7$ that are accessible via temperature [6] and pressure. Starting with the high-symmetry parent structure $I4/mmm$, the condensation of $a^0a^0c^-$, $a^-a^-c^0$, and $a^0a^0c^+$ octahedral rotation patterns leads to structures with *Acaa*, *Amam*, and *Acam* symmetries, respectively. The symmetries of these octahedral rotations are given by irreducible representations of $I4/mmm$ as indicated. Combining the $a^-a^-c^0$ and $a^0a^0c^+$ rotations leads to the polar $A2_1am$ structure, whereas combining $a^-a^-c^0$ and $a^0a^0c^-$ rotations leads to the *Pnab* structure. In each of these structures, a third distortion, primarily consisting of Sr displacements, is induced by a coupling to the octahedral rotations. In $A2_1am$, there is a net Sr displacement in each perovskite layer (green arrows), leading to a polarization, whereas in *Pnab* the displacements in each layer cancel (blue arrows).

Infrared spectroscopy is a sensitive, microscopic technique for unraveling symmetry-breaking in materials. This is because different structural phases will have dissimilar vibrational mode patterns, and variations in these patterns reflect symmetry changes. At the same time, the technique reveals specific local lattice distortions. This means that a careful analysis of the phonons allows us to discriminate between phases with different space groups [16–20]. The challenge, of course, is to cover the full infrared frequency range—including the far infrared. The latter is well-known to have low-signal levels even before a diamond anvil cell is incorporated into the setup. One way to overcome this challenge is to combine diamond anvil cell techniques with a high-brightness synchrotron source [21]. By so doing, we can explore the lattice dynamics of $Sr_3Sn_2O_7$ under compression with enough sensitivity to discriminate between different symmetry candidates. Finally, $Sr_3Sn_2O_7$ is softer than many other hybrid improper ferroelectrics, and as a result, the structural transitions are likely to take place at overall lower-energy scales.

In order to explore the properties of hybrid improper ferroelectrics under external stimuli, we measure the infrared response of $Sr_3Sn_2O_7$ as a function of pressure and compare our findings to complementary lattice dynamics calculations. We show that infrared spectroscopy is an effective diagnostic for the detection of pressure-induced phase transitions in solids. In addition to the ferroelectric phase, we find that three additional structural phases are accessible under compression at room temperature. We identify the symmetry of each phase by comparing the pattern and shape of the vibrational spectrum with predictions computed for several different candidate space groups. Based upon these correlations and an analysis of the displacement patterns, we reveal which structural order parameters change as compression transforms one phase into another. The overall sequence of pressure-induced transitions that we observe in $Sr_3Sn_2O_7$ is $A2_1am \leftrightarrow Pnab \leftrightarrow Acaa \leftrightarrow I4/mmm$. Comparison with related work on other hybrid improper ferroelectrics [22] including $Ca_3Ti_2O_7$, $Ca_3Mn_2O_7$, and $Sr_3Zr_2O_7$ as well as variable temperature studies of $Sr_3Sn_2O_7$ leads to a set of structure-property relations that reveal precisely how and why these sequences occur. Remarkably, we demonstrate that temperature and pressure are essentially interchangeable tuning parameters in $Sr_3Sn_2O_7$; both drive across the entire series of transitions. The advantage of pressure (and very likely strain [23]) is that all of the phases can be accessed at room temperature (rather than going to 900 or 1000 K), which bodes well for applications of this interesting class of materials.

II. METHODS

A. Sample growth and spectroscopic methods

High-quality $Sr_3Sn_2O_7$ single crystals were grown using optical floating zone techniques as described previously [13]. A carefully chosen flake of the crystal (on the order of the gasket size) was loaded into a symmetric diamond anvil cell along with a pressure medium and an annealed ruby ball. Care was taken to optimize optical density in order to reveal the excitations of interest. It is important to maintain a hydrostatic or quasihydrostatic environment within the diamond anvil cell over the full pressure range of interest. We therefore take great care loading the cell to avoid sample bridging between diamonds [24] with a properly-sized gasket (100 μm for 400 μm diamond anvils) and an appropriate pressure medium. In this case, petroleum jelly was used as a pressure medium to assure a quasihydrostatic environment. The position of the $R1$ emission line of ruby was used to determine the pressure with a precision of two full significant figures after the decimal place [25]. We also monitor the shape of the ruby fluorescence spectrum to assure that the sample remains in a quasi-hydrostatic environment [19]. Infrared spectroscopy (50–650 cm^{-1}; 4 cm^{-1} resolution; transmittance geometry) was carried out under pressure using the COMPRES 22-IR-1 beamline at the National Synchrotron Light Source II at Brookhaven National Laboratory. Absorbance is calculated as $\alpha(\omega) = -\ln(\mathcal{T}(\omega))$, where $\mathcal{T}(\omega)$ is the measured transmittance. All data were collected at room temperature. For comparison, we also performed traditional infrared absorption measurements at ambient conditions using a Bruker 113v spectrometer equipped with a bolometer (20–700 cm^{-1}; 2 cm^{-1} resolution). Mode assignments were made by comparison with literature data [9] and our lattice dynamics calculations as described in the text.

B. Theoretical methods

We performed density functional theory (DFT) [26] calculations using the projector augmented wave (PAW) [27] method as implemented in VASP [28]. We used the PBEsol exchange-correlation functional [29], a 600 eV plane-wave cutoff, and a 2 meV/Å force convergence criterion. All structural relaxations were performed in a 48-atom computational cell, for which we used a $6 \times 6 \times 2$ Monkhorst-Pack [30] k-point mesh. For the $Ca_3Mn_2O_7$ calculation presented in Table I, we employed DFT+U [31] with the U and J values on Mn set to 4.5 and 1 eV, respectively [2].

The Γ point phonon frequencies were computed using density functional perturbation theory (DFPT) [32–34]. These calculations were performed in primitive unit cells, which contained 12, 24, or 48 atoms depending on the structural symmetry. For the 24 and 12 atom cells, we used $4 \times 4 \times 6$ and $6 \times 6 \times 6$ k-point meshes, respectively. We computed the infrared-active phonon intensities using Phonopy-Spectroscopy [35], where the intensity of the mth phonon is given by

$$I_{IR}(m) = \sum_{\alpha} \left| \sum_{\kappa} \sum_{\beta} Z^*_{\kappa,\alpha\beta} X_{\kappa,\beta}(m) \right|^2 . \quad (1)$$

Here $\alpha, \beta = 1, 2, 3$, and $Z_{\kappa,\alpha\beta}$ and $X_{\kappa,\beta}$ are the Born effective charge tensor and eigendisplacement of atom κ, respectively. Born effective charges and the phonon eigenvectors were extracted using PHONOPY [36,37]. We used the ISOTROPY software suite [38] and Bilbao Crystallographic server [39] for group theoretic analysis, and VESTA [40] for the visualization of crystal structures.

III. RESULTS AND DISCUSSION

A. Infrared properties of $Sr_3Sn_2O_7$

Figure 2(a) summarizes the infrared response of $Sr_3Sn_2O_7$ and our vibrational mode assignments. Both traditional infrared absorption and spectra taken using a diamond anvil cell are shown. A group theoretical analysis of the $A2_1am$ structure reveals 72 zone-center phonons (24 atoms in the primitive cell) which transform as

$$\Gamma = \underbrace{A_1 \oplus B_1 \oplus B_2}_{\text{Acoustic}} \oplus 17A_2 \oplus \underbrace{\underbrace{18A_1 \oplus 16B_1 \oplus 18B_2}_{IR}}_{\text{Raman}} . \quad (2)$$

We assign the spectral features of $Sr_3Sn_2O_7$ as indicated in Fig. 2(a) using our first-principles lattice dynamics calculations. In making these assignments, we prioritize the frequency pattern, intensity, and clustering trends from the calculations. This approach is consistent with the type of analyses that already appears in the literature [16–19]. In several cases, mode symmetries are grouped to indicate collective contributions to a particular peak. A complete list of mode assignments is given in Table S2 within the Supplemental Material [41].

Figures 2(b) and 2(d) displays the infrared spectra of $Sr_3Sn_2O_7$ as a function of pressure. There are a number of peaks that appear, disappear, shift, and split. Examples are labeled α - γ. These features provide a basis for determining critical pressures. For instance, the appearance of the 225 cm^{-1} feature (β) and the reduction of the 110 cm^{-1} structure above approximately 2 GPa indicates the development of a high-pressure phase, which we label HP1. To determine the symmetry of HP1, we analyze several different candidate space groups and calculations of their phonons, comparing these predictions with the experimental spectrum. This process is detailed in the next section. The 225 cm^{-1} feature disappears again near 15 GPa, indicative of a second structural phase transition. The 280 cm^{-1} mode (γ) behaves similarly. It develops a shoulder around 270 cm^{-1} at 2 GPa which disappears after 15 GPa, providing further evidence for a distinct structural phase, henceforth called HP2. At the same time, the 150 cm^{-1} mode (α) hardens in HP1 before softening slightly in HP2. Moreover, the feature near 330 cm^{-1} blue shifts under compression, splits weakly in HP1, comes back together in HP2, and softens and diminishes in the final phase (HP3). The signature of HP3 is subtle. It includes (i) a number of peaks converging near 320 cm^{-1}, which causes an apparent "narrowing" of this structure [Fig. 2(b)], and (ii) several vibrational modes (especially at 165 and 178 cm^{-1}) shifting across the transition regime [Fig. 2(c)]. The color scheme in Fig. 2(b)

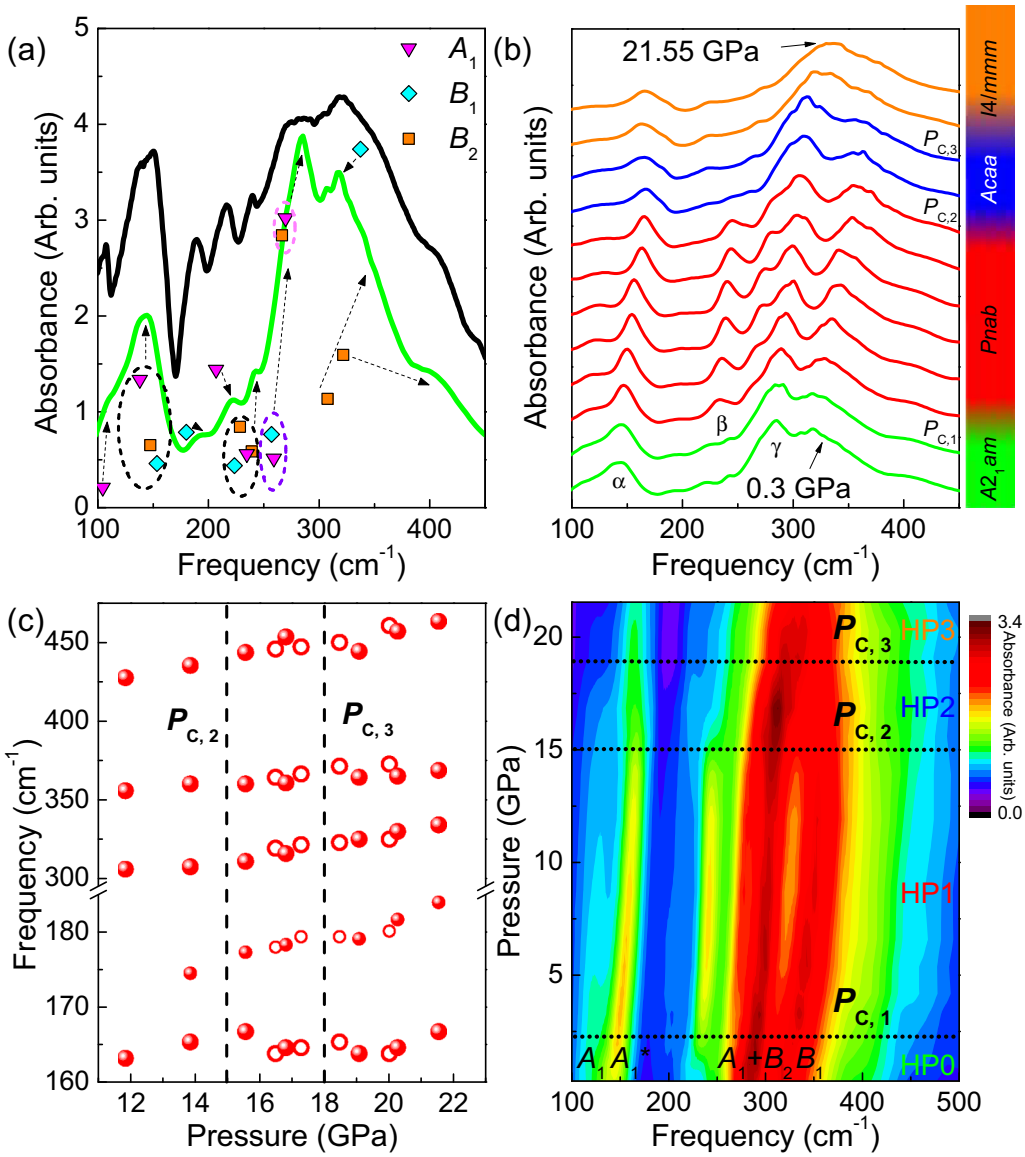

FIG. 2. (a) Infrared response of $Sr_3Sn_2O_7$ measured using traditional spectroscopic techniques at 300 K (black) and inside the diamond anvil cell at ambient pressure (green). Colored symbols indicate predicted mode positions, symmetries, and intensities. (b) Infrared response of $Sr_3Sn_2O_7$ under pressure at room temperature. The curves are offset for clarity only. The color scheme denotes the four structural phases. The labels α, β, and γ indicate the 150, 225, and 280 cm^{-1} features, respectively, as mentioned in the text. (c) Frequency vs pressure plot of selected modes that show the critical pressures $P_{C,2}$ and $P_{C,3}$. The filled and open circles denote separate runs. Error bars are on the order of the symbol size. (d) Contour plot of the data in panel (b). The vibrational features of the ambient pressure phase and the critical pressures are labeled.

captures these four distinct structural phases. We label the critical pressure as $P_{C,1}$, $P_{C,2}$, and $P_{C,3}$.

Figure 2(d) summarizes these findings in the form of a contour plot. Mode symmetries are also indicated according to our assignments for the $A2_1am$ phase [Fig. 2(a)]. Based upon the appearance, disappearance, and frequency shifts of various vibrational modes under compression, the critical pressures of $Sr_3Sn_2O_7$ are 2, 15, and 18 GPa. As we shall see below, the trends across $P_{C,1}$ are not those of a simple group-subgroup relationship, although those at $P_{C,2}$ and $P_{C,3}$ do follow group-subgroup relations. The transition at $P_{C,3}$ corresponds to a restoration of the aristotype $I4/mmm$ symmetry.

B. Understanding the symmetry of the high-pressure phases

In order to identify the symmetries of these high-pressure states, we combine group theoretic methods and first-principles lattice dynamics calculations to explore a range of possible structural phases of $Sr_3Sn_2O_7$. We select candidate phases by noting that formally, the X_3^-, X_2^+, and X_1^- octahedral rotation distortions shown in Fig. 1 are described by two-dimensional order parameters [42]. We thus consider all space groups generated by distinct directions of these order parameters, as well as their combinations. The entire set of phases that we consider is shown in Fig. S1 within the Supplemental Material [41].

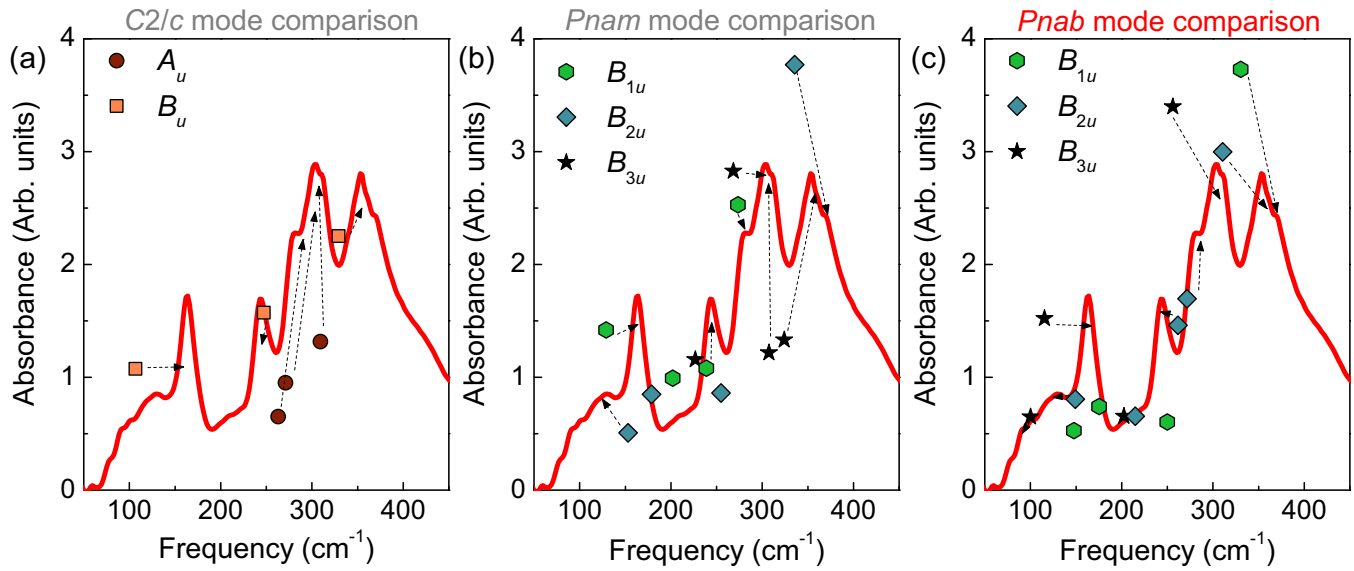

FIG. 3. Infrared spectrum of $Sr_3Sn_2O_7$ in the HP1 high-pressure phase at 11.9 GPa compared with computed mode positions, symmetries, and intensities for three candidate space groups. The space groups considered are: (a) $C2/c$, (b) *Pnam*, and (c) *Pnab*. *Pnab* provides the superior match in terms of most prominent features and overall pattern—as indicated by the heading in red.

We then perform structural relaxations of $Sr_3Sn_2O_7$ with the symmetry constrained to each of the space groups shown in Fig. S1 within the Supplemental Material [41]. As expected, we find the $A2_1am$ structure has the lowest energy. We find that the lowest-energy structures above $A2_1am$ have symmetries *Pnam*, *Pnab*, and $C2/c$. The *Pnam* structure exhibits an $a^-a^-c^+$ rotation pattern as found in $A2_1am$, except that the "sense" of the in-phase rotation is reversed across the rocksalt layer. This phase is known to occur locally as "stacking" domain walls [42] in the $A2_1am$ phase. Both *Pnab* and $C2/c$ host an $a^-a^-c^-$ rotation pattern (with the difference between them being the rotation "sense" across the rocksalt layer). As noted above, *Pnab* has been observed above 410 K in the x-ray diffraction of $Sr_3Zr_2O_7$ and $Sr_3Sn_2O_7$ [5,6]. To check the effect of pressure on the energetics of these low-energy phases, we perform calculations as a function of increasing pressure for each structural phase. At each pressure, we calculate the difference in enthalpy between each of these phases and $A2_1am$ ($\Delta H = \Delta E + P\Delta V$) [43–46]. These results are shown in Fig. S2 within the Supplemental Material [41]. We find that the enthalpy difference between our identified low-energy structures (*Pnam*, *Pnab*, and $C2/c$) and $A2_1am$ decreases slightly (but remains positive) as a function of increasing pressure. Thus, in contrast with our experimental results, we do not see a transition from $A2_1am$ to a different symmetry phase under pressure in DFT. This could be because the octahedral rotation amplitudes calculated with these methods are larger than those in the experimental structure (see Table I), or because our calculations are at 0 K while the experiments are performed at room temperature. Nevertheless, these calculations still provides a useful set of candidate space groups against which we can test our spectra.

For each of these low-energy phases we calculate the phonons and infrared intensities in order to identify the symmetry of HP1. We assign spectral features by comparing our theoretically predicted mode positions, patterns, and intensities with the experimental spectrum. As an example of this procedure, we overlaid the infrared spectrum of $Sr_3Sn_2O_7$ at 11.9 GPa with the calculated mode positions and intensities of the different candidate space groups for the HP1 phase (Fig. 3). While $C2/c$ and *Pnam* are in reasonable agreement with the measured spectrum, the calculated mode pattern for *Pnab* symmetry provides superior agreement in terms of mode intensities and clustering patterns, particularly the presence of low frequency B_{3u} mode and a clearer correspondence of infrared mode intensities around 200 cm^{-1}. We therefore assign the symmetry of the HP1 phase of $Sr_3Sn_2O_7$ to be *Pnab*. In addition to providing a superior match in terms of the most prominent features and overall pattern under pressure, this nonpolar space group is consistent with variable temperature infrared reflectance (Fig. S3 within the Supplemental Material [41]) and Raman scattering [11,12]. One important aspect of the $A2_1am \leftrightarrow$ *Pnab* transition is that these space groups do not have a group-subgroup relationship, as can be seen from the symmetry group tree in Fig. S1 within the Supplemental Material [41]. This behavior is indicative of a first-order phase transition. The same discontinuous transition has been observed in $Sr_3Sn_2O_7$ and $Sr_3Zr_2O_7$ [5,6] with increasing temperature.

To further search for signatures of this phase transition, we also use our first principles lattice dynamics calculations to check the pressure evolution of low-frequency phonons in the $A2_1am$ phase. Our approach is motivated by the soft mode theory of structural phase transitions [47–49]. This theory has been most widely applied to understanding displacive ferroelectric transitions, where a phonon softens to zero frequency at the transition point. However, soft modes also can be present in discontinuous transitions albeit with a finite frequency at the transition point [49]. Our calculations

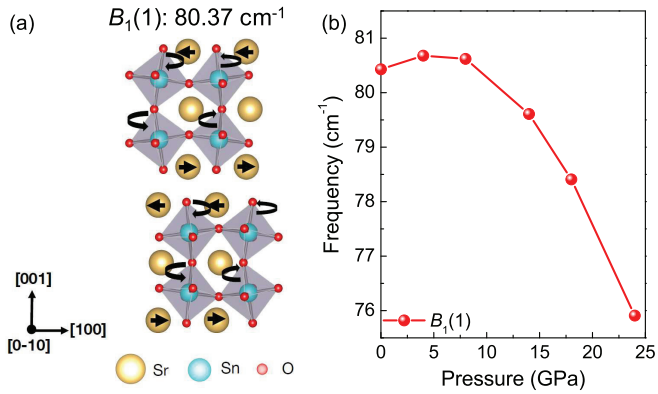

FIG. 4. (a) Main atomic motions that contribute to the $B_1(1)$ phonon of $Sr_3Sn_2O_7$ in the $A2_1am$ structure. (b) Predicted evolution of the frequency of the $B_1(1)$ phonon with pressure.

on $Sr_3Sn_2O_7$ reveal one low-frequency phonon (80.37 cm^{-1}) with B_1 symmetry that softens slightly under increasing pressure [Fig. 4(b)]. Visualizing the displacement pattern of this phonon [Fig. 4(a)], we find that it consists primarily of Sr displacements and an out-of phase $a^0a^0c^-$ octahedral rotation, which are very similar to the M_5^+ and X_1^- distortions in *Pnab*, respectively. This observation further supports our assignment of *Pnab* symmetry to the HP1 phase, although this particular mode is not observed in the experimental spectra due to the limitations of our technique. We note that a similar finite frequency phonon softening was observed at a pressure induced phase transition in $GdVO_4$ [50].

We take a similar approach to identify the symmetry of the HP2 and HP3 phases. From the space groups shown in Fig. S1 within the Supplemental Material [41], we choose to consider structures where one or both of the octahedral rotations in *Pnab* is removed: *Amam* ($a^-a^-c^0$), *Acaa* ($a^0a^0c^-$), and $I4/mmm$ (no rotations). We also consider $P4_2/mnm$, which consists of $a^-b^0b^0$ and $b^0a^-b^0$ octahedral rotations in alternating perovskite slabs and is known to be stabilized in other $n = 2$ Ruddlesden-Popper materials by chemical substitution [51]. Like *Amam*, the $P4_2/mnm$ structure is established by the X_3^- irreducible representation, except the order parameter is in a symmetry distinct direction [42]. Our calculations (Fig. S2 within the Supplemental Material [41]) show that of these phases, *Amam* has the lowest enthalpy at low pressures, whereas at higher pressures *Acaa* has lower enthalpy, and in fact the enthalpy difference $H_{Acaa} - H_{A2_1am}$ becomes negative above $\approx$ 20 GPa. We then compared the phonon frequencies and infrared intensities calculated for each of these candidate space groups with the measured spectrum at 16.85 GPa (Fig. S4 within the Supplemental Material [41]). We notice that while $I4/mmm$ provides a poor match, $P4_2/mnm$, *Amam*, and *Acaa* are good candidates. Focusing on the finer details and the low-frequency peaks, we find that theory and experiment agree slightly better for *Acaa* than *Amam* and $P4_2/mnm$. This, together with our calculations indicating a negative enthalpy difference $H_{Acaa} - H_{A2_1am}$ at a slightly higher pressure, leads us to assign *Acaa* symmetry to the HP2 phase. Finally, to find the symmetry of HP3, we again compare the $I4/mmm$, *Amam*, and *Acaa* theoretical intensities with the experimental spectrum obtained at 21.55 GPa as shown in Fig. S5 within the Supplemental Material [41]. Our analysis suggests a close agreement with $I4/mmm$. We expect the transitions to HP2 and HP3 to be second-order because they follow a group-subgroup relationship and occur over a range. The overall sequence of transitions in $Sr_3Sn_2O_7$ under pressure is therefore $A2_1am \leftrightarrow Pnab \leftrightarrow Acaa \leftrightarrow I4/mmm$. This is exactly the same sequence of phases observed with increasing temperature in $Sr_3Sn_2O_7$ [6].

C. Structure-property relations in $n = 2$ Ruddlesden-Popper hybrid improper ferroelectrics

In the previous sections, we identify the critical pressures and corresponding phase transitions in $Sr_3Sn_2O_7$ using a combination of high-pressure infrared spectroscopy, group theoretic analysis, and lattice dynamics calculations. Here, we more broadly examine the pattern of structural distortions and phase transitions under external stimuli in a larger class of $n = 2$ Ruddlesden-Popper compounds.

We begin by comparing the pressure dependence of $Sr_3Sn_2O_7$ with other members of the $n = 2$ Ruddlesden-Popper series. Subtle differences related to the evolution of the structural order parameters impact how each system departs from $A2_1am$ symmetry [52]. In $Ca_3Ti_2O_7$, inelastic neutron scattering reveals that the X_2^+ octahedral rotation is significantly more sensitive to pressure than the X_3^- rotation [53]. Interestingly, the opposite is true in the Mn counterpart; the $a^-a^-c^0$ rotation is more responsive to compression than the $a^0a^0c^+$ rotation [54]. $Ca_3Ti_2O_7$ is also overall stiffer than $Ca_3Mn_2O_7$ as evidenced by the phonon behavior across the critical pressure [55]. In both cases, the polar $A2_1am$ ground state is lost between 5 and 8 GPa with the transition range in the Mn analog being somewhat narrower (between 5 and 6 GPa). Therefore, $Ca_3Ti_2O_7$ and $Ca_3Mn_2O_7$ only have a single critical pressure within the range investigated thus far [55], although additional transitions are anticipated and negative thermal expansion is predicted [8] at significantly higher pressures.

As discussed above, $Sr_3Sn_2O_7$ negotiates the same sequence of phases under both compression and temperature. Given this analogy, we next examine the temperature-dependent structural phase transitions for various materials across the $n = 2$ Ruddlesden-Popper series. We begin by noting that the sequence of temperature-dependent phase transitions in $Sr_3Zr_2O_7$ is remarkably similar to the temperature (and pressure) transitions in $Sr_3Sn_2O_7$ [5,6]. A combination of x-ray diffraction, second harmonic generation, and theoretical analysis reveals that $Sr_3Zr_2O_7$ undergoes the same first-order $A2_1am \leftrightarrow Pnab$ transition as $Sr_3Sn_2O_7$, although the transition temperature is higher (approximately 700 K compared to 400 K in $Sr_3Sn_2O_7$). With increasing temperature, one of the rotations turns off, although the two materials differ in the following respect: in $Sr_3Sn_2O_7$ there is a transition to *Acaa* ($a^0a^0c^-$ rotations) at 700 K, whereas in $Sr_3Zr_2O_7$ there is a transition to *Amam* ($a^-a^-c^0$ rotations) at 900 K. Finally, both materials go into the high-symmetry $I4/mmm$ phase above 1000 K. These higher-temperature transitions are second order [5,6].

TABLE I. Tolerance factor and amplitudes of the X_3^- and X_2^+ octahedral rotations for selected $n = 2$ members of the Ruddlesden-Popper series. The octahedral rotation amplitudes are obtained by decomposing ambient pressure $A2_1am$ structures with respect to the high-symmetry $I4/mmm$ structure, and are reported for a 24-atom cell in units of Å. The tolerance factors were calculated using A-O and B-O bond lengths obtained from the bond valence model [57–59], assuming 12- and 6-fold coordination for the A and B cations, respectively. The experimental values—except the P_C for $Sr_3Sn_2O_7$ reported in this work—were obtained from literature [5,6,60–63].

Material	Tolerance factor	X_3^- (DFT)	X_2^+ (DFT)	X_3^- (Expt)	X_2^+ (Expt)	P_C (GPa)	T_C (K)
$Sr_3Zr_2O_7$	0.942	1.27	0.86	1.07	0.78		700
$Ca_3Ti_2O_7$	0.946	1.20	0.87	1.01	0.83	5–8	1100
$Sr_3Sn_2O_7$	0.957	1.18	0.76	0.89	0.67	2	400
$Ca_3Mn_2O_7$	0.977	0.87	0.79	0.66	0.73	5–6	270–320

Expanding the comparison to a broader set of $n = 2$ Ruddlesden-Popper materials reveals that the number and symmetries of the high-temperature phases varies with composition [5]. That said, the tolerance factor τ, defined as $\tau = \frac{r_{A-O}}{\sqrt{2}(r_{B-O})}$, where r_{A-O} and r_{B-O} are the B-O and A-O bond lengths respectively, is a useful quantity for formulating trends [56]. In fact, Yoshida *et al.* identified a relationship between the tolerance factor τ and the Curie temperature T_C which holds across many chemical compositions [5]. One clear take-away is that materials with smaller tolerance factors have a higher T_C. From a structural viewpoint, this makes sense because materials with smaller tolerance factors have larger octahedral rotation amplitudes (Table I). Since the phase transitions in these $n = 2$ Ruddlesden-Popper materials all involve changes to the octahedral rotations, it takes more energy (higher temperature) to drive the transition in the low-tolerance factor compounds.

Inspired by these results, we decided to investigate whether the tolerance factor can serve as a similar descriptor for pressure-driven transitions in this family of materials. Unfortunately, the situation is not so simple. From our discussion above, we note that of the systems for which there is available data, $Sr_3Sn_2O_7$ has the lowest critical pressure ($P_{C,1}$). The critical pressures of $Ca_3Mn_2O_7$ and $Ca_3Ti_2O_7$ are somewhat higher. Consulting Table I, we see that $Ca_3Ti_2O_7$ has a smaller tolerance factor (and correspondingly larger octahedral rotation amplitudes) than $Sr_3Sn_2O_7$, thus this pair of materials suggests a critical pressure-tolerance factor trend similar to the temperature-dependent result discussed above. However, $Ca_3Mn_2O_7$, with the largest tolerance factor, is out of line with this trend. We hypothesize that the different B-site chemistry of $Ca_3Mn_2O_7$ (partially filled d shells), may play a role in this difference. We note that studies of ABO_3 perovskites demonstrate that B-site chemistry (in particular partially-filled d shells) influences the pressure response [64].

Another way to organize the data is to analyze trends based upon both the A and B site chemistry. The limited number of experimental results on polar ↔ nonpolar transitions in hybrid improper ferroelectrics under pressure makes it challenging to reach firm conclusions. Here we explore some potentially important factors based on the presently available data, which may be refined as more experimental results become available in the future. The similar evolution of phases with temperature in $Sr_3Sn_2O_7$ and $Sr_3Zr_2O_7$ suggests grouping materials based on their A-site cation, which is consistent with the role of the A-site in determining size effects, bonding preferences [65], and compressibility [14]. Based on this similarity, it is plausible that $Sr_3Zr_2O_7$ may show a similar sequence of phase transitions under pressure as those observed in $Sr_3Sn_2O_7$. If so, synchrotron-based infrared work in a diamond anvil cell would allow structure-property comparisons with $Sr_3Sn_2O_7$ to be developed. Turning to the two Ca-containing materials, we note that P_C of $Ca_3Ti_2O_7$ is higher than that of $Ca_3Mn_2O_7$ (Table I), suggesting a possible P_C-tolerance factor relation within a subset of materials with the same A cation, although lacking data on additional compounds we cannot make a definitive statement on this trend.

We next explore the possibility of trends based on the B-site cation. The four materials in Table I all have different B-site cations, of which one is a p-block element (Sn), one has a partially filled d shell (Mn), and two have formally empty d orbitals (Ti, Zr). Considering the octahedral rotation amplitudes in Table I, we note that the amplitude of the X_3^- rotation increases monotonically with decreasing tolerance factor, whereas the X_2^+ rotation amplitude in $Sr_3Sn_2O_7$ is anomalously small given its tolerance factor. This could be connected to Sn being a p-block element and its relatively low P_C. $Sr_3Zr_2O_7$ and $Ca_3Ti_2O_7$ both have larger X_2^+ and X_3^- order parameter amplitudes. This is largely due to their lower tolerance factors [6], although their similar B-site chemistry also could play a role. This B-site relationship may lead to similar evolution of structural order parameters with pressure, although clearly one needs to measure to much higher levels of compression for $Ca_3Ti_2O_7$. In contrast, with its partially filled d-shell $Ca_3Mn_2O_7$ is likely to undergo a different sequence of structural distortions with the suppression of the X_3^- rotation being more important [54].

We therefore propose three significant factors that together determine the pressure response for a particular $n = 2$ Ruddlesden-Popper material: (i) the tolerance factor, with smaller tolerance factor compounds having higher critical pressures; (ii) the A-site occupation which appears to be primarily a size effect; and (iii) the B-site chemistry. The tolerance factor seems to determine the phase transition range and critical temperature/pressure within the same set of A-site compounds, whereas B-site chemistry governs the development of structural order parameters and in turn the progression of phase transitions according group-subgroup relationships. Further pressure-dependent studies on a broader suite of $n = 2$ Ruddlesden-Popper materials would allow further refinement of these relationships. The overall lower-critical pressures of $Sr_3Sn_2O_7$ compared to the other materials,

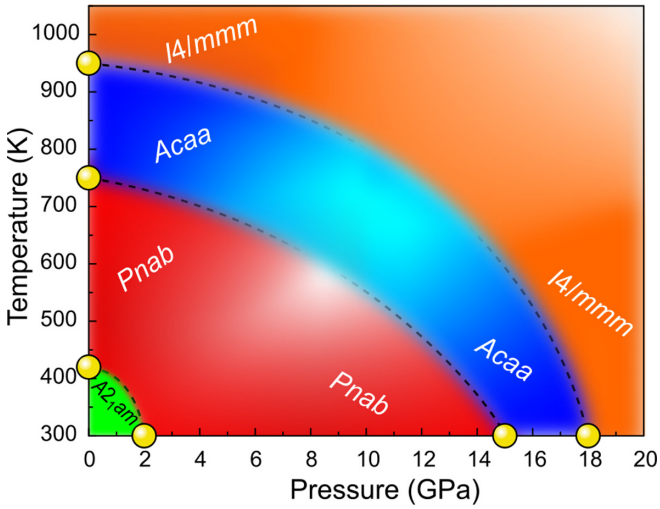

FIG. 5. Schematic temperature-pressure (T - P) phase diagram of $Sr_3Sn_2O_7$ developed from the critical pressures identified in this work as well as the critical temperatures from literature [5]. These values are indicated by yellow spheres. Error bars are on the order of symbol size. Blurring indicates uncertainly in the position and shape of the phase boundaries—especially in the intermediate temperature and pressure regime.

makes it more amenable to physical tuning and appealing for applications.

D. Developing the schematic temperature-pressure phase diagram of $Sr_3Sn_2O_7$

To further explore connections between the temperature- and pressure-induced phase transitions in $Sr_3Sn_2O_7$, we construct a schematic temperature-pressure (T-P) phase diagram in Fig. 5. The transition temperatures are taken from previous structural studies [6,12], and the pressure-driven transitions are from the present work. We draw the phases boundaries between these points using a typical asymptotic dependence near the critical values. They are blurred to indicate uncertainty. The intermediate temperature-pressure regime is also blurred—again to indicate uncertainty.

Figure 5 highlights how both temperature and pressure instigate the same $A2_1am \leftrightarrow Pnab \leftrightarrow Acaa \leftrightarrow I4/mmm$ sequence of transitions. There is thus an unexpected compatibility and commutability of tuning parameters even though (i) we do not know the details of how the phase boundary lines evolve at intermediate temperatures and pressures and (ii) there is no simple energy equivalence between these two quantities. The crucial difference is that pressure (and very likely strain) access these phases and their functionalities at room temperature—an essential characteristic of viable applications. A similar temperature/pressure correspondence may be present in other hybrid improper ferroelectrics.

We note that the equivalence between the sequence of phases accessed with pressure and temperature in $Sr_3Sn_2O_7$ is unusual; typically temperature and pressure have opposite effects because increasing temperature results in thermal expansion and increasing pressure induces volume contraction. That said, a similar temperature/pressure phase transition equivalence has been observed in perovskite $LaAlO_3$ [66,67] despite its positive thermal expansion [68], which can be attributed to the BO_6 octahedra being more compressible than the AO_{12} polyhedra [15,69]. In particular, perovskites with more compressible BO_6 octahedra generally exhibit a negatively sloped phase boundary in the P-T phase diagram and opposite sign changes of entropy and volume ($\Delta S > 0$, $\Delta V < 0$) [15]. Figure 5 displays such a negative phase boundary, and we hypothesize that a similar mechanism may underlie the pressure/temperature behavior of $Sr_3Sn_2O_7$.

IV. SUMMARY AND OUTLOOK

Hybrid improper ferroelectrics like $Sr_3Sn_2O_7$ are well recognized for the complex interplay between different order parameters and structural phases. In order to explore this phase competition in greater detail, we brought together diamond anvil cell techniques, synchrotron-based infrared spectroscopy, symmetry analysis, and lattice dynamics calculations to reveal the sequence of compression-induced structural phase transitions. By comparing the pattern and shape of the vibrational spectrum with predictions computed for several different candidate space groups, we reveal that the overall sequence of pressure-induced transitions in $Sr_3Sn_2O_7$ is $A2_1am \leftrightarrow Pnab \leftrightarrow Acaa \leftrightarrow I4/mmm$. We anticipate that this paper will motivate complementary high-pressure x-ray measurements to confirm the space group sequence. Comparing our findings with related work on other hybrid improper ferroelectrics including $Ca_3Ti_2O_7$, $Ca_3Mn_2O_7$, and $Sr_3Zr_2O_7$ as well as variable temperature studies of $Sr_3Sn_2O_7$ leads to a set of structure-property relations that may be useful in understanding the sequence of transitions more broadly. Perhaps the most remarkable aspect of this analysis is the finding that pressure is comparable to temperature in terms of the sequence of ferroelectric and structural phases. This may be because adding energy to the system—in the form of increased temperature or compression—simply triggers a common set of order parameters. There are, of course a number of advantages to pressure and strain-driven functionality at room temperature—not the least of which is that it obviates the need for ultra-high temperatures. Similar effects may be present in other members of the hybrid improper ferroelectrics family. Looking forward, we suggest that by combining multiple knobs for tuning between polar and nonpolar states, for example chemical substitution and pressure, exquisite control over the energy difference between the competing polar and nonpolar states may be achievable. This holds particular interest for the realization of new antiferroelectrics, for which a nonpolar ground state with a polar phase slightly higher in energy is required. We suggest that these $n = 2$ Ruddlesden-Popper materials may find room-temperature application in lead-free antiferroelectric devices.

ACKNOWLEDGMENTS

Research at the University of Tennessee is supported by the Materials Science Division, Office of Basic Energy Sciences, U.S. Department of Energy, under award DE-FG02-01ER45885. Work at Rutgers University is supported by the NSF-DMREF program (DMR-1629059). Work at the

National Synchrotron Light Source II at Brookhaven National Laboratory was funded by the Department of Energy (DE-AC98-06CH10886). Use of the 22-IR-1 beamline was supported by COMPRES under NSF Cooperative Agreement EAR 1606856 and CDAC (DE-NA0003975). This research used computational resources supported by Center for Functional Nanomaterials, which is a U.S. DOE Office of Science Facility, at Brookhaven National Laboratory under Contract No. DE-SC0012704. We thank Feng Ye for useful discussions.

[1] E. Bousquet, M. Dawber, N. Stucki, C. Lichtensteiger, P. Hermet, S. Gariglio, J.-M. Triscone, and P. Ghosez, Nature (London) **452**, 732 (2008).
[2] N. A. Benedek and C. J. Fennie, Phys. Rev. Lett. **106**, 107204 (2011).
[3] Y. S. Oh, X. Luo, F.-T. Huang, Y. Wang, and S.-W. Cheong, Nat. Mater. **14**, 407 (2015).
[4] Y. Wang, F.-T. Huang, X. Luo, B. Gao, and S.-W. Cheong, Adv. Mater. **29**, 1601288 (2017).
[5] S. Yoshida, K. Fujita, H. Akamatsu, O. Hernandez, A. Sen Gupta, F. G. Brown, H. Padmanabhan, A. S. Gibbs, T. Kuge, R. Tsuji *et al.*, Adv. Funct. Mater. **28**, 1801856 (2018).
[6] S. Yoshida, H. Akamatsu, R. Tsuji, O. Hernandez, H. Padmanabhan, A. Sen Gupta, A. S. Gibbs, K. Mibu, S. Murai, J. M. Rondinelli *et al.*, J. Am. Chem. Soc. **140**, 15690 (2018).
[7] N. A. Benedek, J. M. Rondinelli, H. Djani, P. Ghosez, and P. Lightfoot, Dalton Trans. **44**, 10543 (2015).
[8] F. T. Huang, F. Xue, B. Gao, L. H. Wang, X. Luo, W. Cai, X. Z. Lu, J. M. Rondinelli, L. Q. Chen, and S. W. Cheong, Nat. Commun. **7**, 11602 (2016).
[9] K. A. Smith, E. A. Nowadnick, S. Fan, O. Khatib, S. J. Lim, B. Gao, N. C. Harms, S. N. Neal, J. K. Kirkland, M. C. Martin *et al.*, Nat. Commun. **10**, 5235 (2019).
[10] M. H. Lee, C.-P. Chang, F.-T. Huang, G. Y. Guo, B. Gao, C. H. Chen, S.-W. Cheong, and M.-W. Chu, Phys. Rev. Lett. **119**, 157601 (2017).
[11] J. J. Lu, X. Q. Liu, X. Ma, M. S. Fu, A. Yuan, Y. J. Wu, and X. M. Chen, J. Appl. Phys. **125**, 044101 (2019).
[12] X. Sun, X. Yang, C. Xu, X. Gan, W. Zhang, Z. Gao, H.-L. Cai, and X. Wu, Chem. Phys. Lett. **728**, 74 (2019).
[13] X. Xu, Y. Wang, F. Huang, K. Du, E. A. Nowadnick, and S. Cheong, Adv. Funct. Mater. **30**, 2003623 (2020).
[14] J. Zhao, N. L. Ross, and R. J. Angel, Acta Cryst. B **60**, 263 (2004).
[15] R. J. Angel, J. Zhao, and N. L. Ross, Phys. Rev. Lett. **95**, 025503 (2005).
[16] H.-H. Kung, R. E. Baumbach, E. D. Bauer, V. K. Thorsmolle, W.-L. Zhang, K. Haule, J. A. Mydosh, and G. Blumberg, Science **347**, 1339 (2015).
[17] D. V. S. Muthu, P. Teredesai, S. Saha, Suchitra, U. V. Waghmare, A. K. Sood, and C. N. R. Rao, Phys. Rev. B **91**, 224308 (2015).
[18] K. Kim, S. Y. Lim, J.-U. Lee, S. Lee, T. Y. Kim, K. Park, G. S. Jeon, C.-H. Park, J.-G. Park, and H. Cheong, Nat. Commun. **10**, 345 (2019).
[19] A. Clune, N. Harms, K. R. O'Neal, K. Hughey, K. A. Smith, D. Obeysekera, J. Haddock, N. S. Dalal, J. Yang, Z. Liu, and J. L. Musfeldt, Inorg. Chem. **59**, 10083 (2020).
[20] A. Liang, R. Turnbull, E. Bandiello, I. Yousef, C. Popescu, Z. Hebboul, and D. Errandonea, Crystals **11**, 34 (2020).
[21] G. L. Carr, Rev. Sci. Instrum. **72**, 1613 (2001).
[22] R. Uppuluri, H. Akamatsu, A. Sen Gupta, H. Wang, C. M. Brown, K. E. Agueda Lopez, N. Alem, V. Gopalan, and T. E. Mallouk, Chem. Mater. **31**, 4418 (2019).
[23] X.-Z. Lu and J. M. Rondinelli, Nat. Mater. **15**, 951 (2016).
[24] P. Wang, D. He, C. Xu, X. Ren, L. Lei, S. Wang, F. Peng, X. Yan, D. Liu, Q. Wang, L. Xiong, and J. Liu, J. Appl. Phys. **115**, 043507 (2014).
[25] H. K. Mao, J. Xu, and P. M. Bell, J. Geophys. Res. **91**, 4673 (1986).
[26] P. Hohenberg and W. Kohn, Phys. Rev. **136**, B864 (1964).
[27] P. E. Blöchl, Phys. Rev. B **50**, 17953 (1994).
[28] G. Kresse and J. Furthmüller, Phys. Rev. B **54**, 11169 (1996).
[29] J. P. Perdew, A. Ruzsinszky, G. I. Csonka, O. A. Vydrov, G. E. Scuseria, L. A. Constantin, X. Zhou, and K. Burke, Phys. Rev. Lett. **100**, 136406 (2008).
[30] H. J. Monkhorst and J. D. Pack, Phys. Rev. B **13**, 5188 (1976).
[31] V. I. Anisimov, F. Aryasetiawan, and A. I. Lichtenstein, J. Phys.: Condens. Matter **9**, 767 (1997).
[32] P. Giannozzi, S. de Gironcoli, P. Pavone, and S. Baroni, Phys. Rev. B **43**, 7231 (1991).
[33] X. Gonze and C. Lee, Phys. Rev. B **55**, 10355 (1997).
[34] X. Gonze, Phys. Rev. B **55**, 10337 (1997).
[35] J. M. Skelton, L. A. Burton, A. J. Jackson, F. Oba, S. C. Parker, and A. Walsh, Phys. Chem. Chem. Phys. **19**, 12452 (2017).
[36] A. Togo, F. Oba, and I. Tanaka, Phys. Rev. B **78**, 134106 (2008).
[37] A. Togo, L. Chaput, and I. Tanaka, Phys. Rev. B **91**, 094306 (2015).
[38] B. J. Campbell, H. T. Stokes, D. E. Tanner, and D. M. Hatch, J. Appl. Crystallogr. **39**, 607 (2006).
[39] E. Kroumova, M. Aroyo, J. Perez-Mato, A. Kirov, C. Capillas, S. Ivantchev, and H. Wondratschek, Phase Transitions **76**, 155 (2003).
[40] K. Momma and F. Izumi, J. Appl. Crystallogr. **44**, 1272 (2011).
[41] See Supplemental Material at http://link.aps.org/supplemental/10.1103/PhysRevB.104.064106 for (i) the calculated Γ point phonons of $Sr_3Sn_2O_7$ in the $A2_1am$ phase; (ii) the theoretical analysis of $Sr_3Sn_2O_7$ structural phases included in this work; (iii) the calculated enthalpy differences between candidate structures and the $A2_1am$ ground state as a function of pressure; (iv) the measured reflectance spectra as a function of temperature for $Sr_3Sn_2O_7$; (v) the comparison of theoretical modes considered for the HP2 phase with the measured spectra of $Sr_3Sn_2O_7$ at 16.85 GPa; and (vi) the comparison of theoretical modes considered for the HP3 phase with the measured spectra of $Sr_3Sn_2O_7$ at 21.55 GPa.
[42] E. A. Nowadnick and C. J. Fennie, Phys. Rev. B **94**, 104105 (2016).
[43] J. Kaczkowski, J. Phys. Chem. Solids **134**, 225 (2019).
[44] S. Ehsan, A. Tröster, F. Tran, and P. Blaha, Phys. Rev. Materials **2**, 093610 (2018).

[45] R. G. Amorim, M. Veríssimo-Alves, and J. P. Rino, Comput. Mater. Sci. **37**, 349 (2006).
[46] S. Javaid and M. Javed Akhtar, J. Appl. Phys. **116**, 023704 (2014).
[47] W. Cochran, Adv. Phys. **9**, 387 (1960).
[48] W. Cochran, Adv. Phys. **10**, 401 (1961).
[49] P. Peercy, Solid State Commun. **16**, 439 (1975).
[50] T. Marqueño, D. Errandonea, J. Pellicer-Porres, D. Martinez-Garcia, D. Santamaria-Pérez, A. Muñoz, P. Rodríguez-Hernández, A. Mujica, S. Radescu, S. Achary, C. Popescu, and M. Bettineli, Phys. Rev. B **100**, 064106 (2019).
[51] F.-T. Huang, B. Gao, J.-W. Kim, X. Luo, Y. Wang, M.-W. Chu, C.-K. Chang, H.-S. Sheu, and S.-W. Cheong, npj Quantum Mater. **1**, 16017 (2016).
[52] F. Pomiro, C. Ablitt, N. C. Bristowe, A. A. Mostofi, C. Won, S.-W. Cheong, and M. S. Senn, Phys. Rev. B **102**, 014101 (2020).
[53] F. Ye, J. Wang, J. Sheng, C. Hoffmann, T. Gu, H. J. Xiang, W. Tian, J. J. Molaison, A. M. dos Santos, M. Matsuda, B. C. Chakoumakos, J. A. Fernandez-Baca, X. Tong, B. Gao, J. W. Kim, and S.-W. Cheong, Phys. Rev. B **97**, 041112(R) (2018).
[54] F. Ye (unpublished).
[55] N. C. Harms (unpublished).
[56] V. M. Goldschmidt, Die Naturwissenschaften **14**, 295 (1926).
[57] M. W. Lufaso and P. M. Woodward, Acta Cryst. B **57**, 725 (2001).
[58] I. D. Brown, Chem. Soc. Rev. **7**, 359 (1978).
[59] N. A. Benedek and C. J. Fennie, J. Phys. Chem. C **117**, 13339 (2013).
[60] X. Q. Liu, J. W. Wu, X. X. Shi, H. J. Zhao, H. Y. Zhou, R. H. Qiu, W. Q. Zhang, and X. M. Chen, Appl. Phys. Lett. **106**, 202903 (2015).
[61] M. M. Elcombe, E. H. Kisi, K. D. Hawkins, T. J. White, P. Goodman, and S. Matheson, Acta Cryst. B **47**, 305 (1991).
[62] M. V. Lobanov, M. Greenblatt, E. N. Caspi, J. D. Jorgensen, D. V. Sheptyakov, B. H. Toby, C. E. Botez, and P. W. Stephens, J. Phys.: Condens. Matter **16**, 5339 (2004).
[63] B. Gao, F.-T. Huang, Y. Wang, J.-W. Kim, L. Wang, S.-J. Lim, and S.-W. Cheong, Appl. Phys. Lett. **110**, 222906 (2017).
[64] H. J. Xiang, M. Guennou, J. Íñiguez, J. Kreisel, and L. Bellaiche, Phys. Rev. B **96**, 054102 (2017).
[65] P. M. Woodward, Acta Cryst. B **53**, 32 (1997).
[66] K. A. Müller, W. Berlinger, and F. Waldner, Phys. Rev. Lett. **21**, 814 (1968).
[67] P. Bouvier and J. Kreisel, J. Phys.: Condens. Matter **14**, 3981 (2002).
[68] B. Chakoumakos, D. Schlom, M. Urbanik, and J. Luine, J. Appl. Phys. **83**, 1979 (1998).
[69] T. Tohei, A. Kuwabara, T. Yamamoto, F. Oba, and I. Tanaka, Phys. Rev. Lett. **94**, 035502 (2005).